

Catalytic Cracking of 1,3,5-Triisopropylbenzene and Low-Density Polyethylene over Hierarchical Y Zeolites and Al-SBA-15

Jim Mensah,^[a, b] Penghui Yan,^[c] Aditya Rawal,^[d] Adam F. Lee,^{*, [e]} Karen Wilson,^[e] Neil Robinson,^[f] Michael L. Johns,^[f] Eric Kennedy,^[a] and Michael Stockenhuber^{*, [a]}

Catalytic cracking of high molecular weight hydrocarbons underpins the production of fossil fuels from petroleum vapour and the recycling of polyolefin waste plastic. However, thermal cracking over conventional microporous solid acids is hindered by poor mass-transport. Here we explore the performance of hierarchical H–Y zeolites and Al-SBA-15 for the catalytic cracking of 1,3,5-triisopropylbenzene (1,3,5-TIPB) and low-density polyethylene (LDPE) in a continuous fixed-bed flow reactor. Dealumination by acid washing was used to create hierarchical mesoporosity in H–Y zeolite and modify the solid acidity. Physicochemical properties were studied by X-ray

diffraction (XRD), transmission electron microscopy (TEM), scanning electron microscopy (SEM), gas adsorption, in-situ Fourier transform infrared (FTIR), ex-situ pyridine DRIFT, ²⁹Si and ²⁷Al nuclear magnetic resonance (NMR), and ¹H relaxation and pulsed field gradient (PFG) NMR diffusion studies. Despite weakening acidity, the introduction of hierarchical porosity promotes deep cracking of both feedstocks; HNO₃ dealuminated H–Y produces five times more cumene and benzene from 1,3,5-TIPB, and 33% more benzene and xylenes from LDPE, than the parent H–Y.

Introduction

Plastics are essential domestic and commercial commodities used worldwide on the megaton scale. However, at their end-of-life usage, the vast majority of (currently fossil-derived) plastics end up as waste sent to landfill.^[1] Polyolefins are the most consumed plastics in the world, accounting for 57% of total municipal solid waste. They mainly consist of low-density polyethylene (LDPE), linear low-density polyethylene (LLDPE), high-density polyethylene (HDPE), and polypropylene (PP) used in e.g. pipes, films, packaging and insulation. Mechanical recycling and incineration, which represent the main alternative destinations for plastic waste, result in progressive loss of material properties and/or the release of toxic pollutants, rendering them unattractive solutions for plastic recycling. Thermocatalytic cracking of plastic waste to valuable chemical building blocks (displacing fossil-derived hydrocarbons) offers

reduced environmental impact and improved process economics.^[2]

Thermal cracking is initiated by the homolytic cleavage of polymer backbones at high temperatures under an inert environment, and yields a broad mixture of C₁–C₆₀ hydrocarbons (waxes, oils and gases). In contrast, catalytic cracking proceeds through a carbocation mechanism,^[3] wherein carbocation formation proceeds by abstraction of a hydride ion by a Lewis acid site (generating carbenium ions) or protonation by a Brønsted acid site (generating carbonium ions).^[4] At temperatures < 400 °C, catalytic cracking of plastics dominates thermal cracking.^[5] Manos et al.^[6] studied the influence of zeolite structure on the catalytic cracking of HDPE at 360 °C in a semibatch reactor using HY, HUSY, Beta, H-mordenite and HZSM-5 zeolites, observing fewer light products (C₂–C₅) over the larger-pore-size zeolites compared to the medium-pore-size zeolites. The catalytic cracking of HDPE over amorphous SiO₂–Al₂O₃ (SAHA) and HZSM-5, H-MOR and HUSY zeolites is

[a] Dr. J. Mensah, Prof. E. Kennedy, Prof. M. Stockenhuber
Chemical Engineering, School of Engineering, University of Newcastle, NSW
2308, Australia
E-mail: michael.stockenhuber@newcastle.edu.au

[b] Dr. J. Mensah
Centre for Advanced Materials and Industrial Chemistry, RMIT University,
Melbourne VIC 3000, Australia

[c] Dr. P. Yan
School of Chemical Engineering, University of Queensland, St Lucia, QLD
4072, Australia

[d] Dr. A. Rawal
Mark Wainwright Analytical Centre, University of New South Wales, NSW
2052, Australia

[e] Prof. A. F. Lee, Prof. K. Wilson
Centre for Catalysis and Clean Energy, Griffith University, Gold Coast QLD
4222, Australia
E-mail: adam.lee@griffith.edu.au

[f] Dr. N. Robinson, Prof. M. L. Johns
Department of Chemical Engineering, University of Western Australia, Perth
WA 6009, Australia

Supporting information for this article is available on the WWW under
<https://doi.org/10.1002/cctc.202300884>

© 2023 The Authors. ChemCatChem published by Wiley-VCH GmbH. This is an open access article under the terms of the Creative Commons Attribution Non-Commercial NoDerivs License, which permits use and distribution in any medium, provided the original work is properly cited, the use is non-commercial and no modifications or adaptations are made.

also reported in a fluidised bed reactor between 290–430 °C.^[7] Strong Brønsted acid sites in HUSY favoured bimolecular hydrogen transfer reactions, resulting in a lower olefin:paraffin product ratio (0.4–0.7), but were susceptible to deactivation. Cracking of 1,3,5-TIPB, a model large hydrocarbon, has been used to selectively probe the external surfaces of zeolites and/or determine the accessibility of in-pore acid sites. The desired Brønsted acid catalysed cracking pathway involves three successive dealkylation steps, each of which yields one molecule of propylene and increases the activation barrier towards subsequent dealkylation.^[8] Secondary, undesired products includes butenes (from transalkylation), di-*n*-propyl or mixed propyl benzenes, mixed ethyl propyl benzenes, cymene and coke.^[9] Deep cracking is indicated by isopropylbenzene and benzene formation.^[10] Several zeolites have been studied for 1,3,5-TIPB cracking, including Y,^[11] HZSM-5,^[12] Beta^[13] and core-shell materials^[14] in the temperature range of 300–500 °C. Hierarchical Beta exhibits the best selectivity (90%) to deep cracking products at 500 °C.^[13]

Zeolites are the most widely studied and commercially significant solid acid catalysts, however, their microporous nature hinders mass-transport of large or sterically bulky molecules, such as those prevalent in plastics. Access to in-pore active sites can be enhanced by introducing auxiliary porosity in the form of meso- and/or macropores. Approaches to synthesise hierarchical porous zeolites can be categorised as top-down or bottom-up.^[15] In the former, additional porosity is introduced by the selective extraction of specific framework components (usually Si or Al) from pre-formed microporous zeolites, while in the latter it is introduced through templates during crystallisation of a sol-gel.^[15a] Effective hierarchisation of zeolites requires interconnections between different pore networks to enhance reactant accessibility to active acid sites and hence improve catalytic performance. For example, mesopores increase the number and size of pore mouths and reduce the intracrystalline diffusion length of micropores, as demonstrated for ZSM-5,^[16] Y zeolite,^[17] mordenite^[18] and BEA zeolite.^[19] Dealumination and desilication are established methods of hierarchisation to modify zeolite porosity and acidity (loading and strength).^[20] Acidity and porosity are critical to the activity, stability and selectivity of zeolites in acid-catalysed reactions, and hence controlling these parameters underpins the effective design of hierarchical zeolites. Considering Y zeolites, Jansen et al. investigated the post-synthetic genesis of mesopores by mild hydrothermal, steaming and acid-leaching treatments.^[21] A small number of mesopores are also reported following the dealumination of Y zeolites by ammonium hexafluorosilicate (AFS),^[22] with severe dealumination inducing a significant loss of micropore volume. The use of silicon tetrachloride (SiCl₄) to dealuminate Y zeolite also affects microporosity.^[23] There is evidence that extraframework aluminium (EFAl) species resulting from dealumination modify zeolite acidity; EFAl species produced by SiCl₄ dealumination generate more acidic Y zeolite catalysts than high-temperature steamed analogues.^[24] Moreover, acid-dealuminated Y is reported to possess an interconnected intracrystalline mesoporosity compared to steaming in USY zeolites which produces unconnected mesoporosity.^[25]

Here we explore the impact of post-synthetic treatment of Y zeolite, namely dealumination by acid washing, on the catalytic cracking of 1,3,5-TIPB and LDPE into paraffins, olefins and aromatics. Acidity and mesoporosity are examined in the context of changing Si:Al ratio and corresponding catalytic cracking of LDPE to value-added products. Nitric acid dealuminated zeolite Y shows excellent activity and lifetime in the cracking of 1,3,5-TIPB, and enhanced gasoline selectivity in LDPE cracking compared to conventional microporous Y. The development of auxiliary mesoporosity and concomitant changes in solid acidity species (type, concentration and strength) are discussed, and performance demonstrated in the continuous catalytic cracking of sterically challenging feedstocks.

Results and Discussion

Physicochemical characterisation

Hierarchisation of the parent Y zeolite was attempted through liquid phase dealumination by acid washing, known to introduce mesoporosity to zeolites.^[26] Textural properties of Y zeolites were examined by Ar physisorption (Figure 1, semi-logarithmic isotherms and cumulative pore volume shown in Figure S3). The parent H–Y zeolite displayed a type-I isotherm as previously reported,^[27] while the treated zeolite displayed a type-IV isotherm.^[28] The presence of large mesopores is indicated by type H4 hysteresis in the adsorption and desorption branches of USY and DA(HNO₃0.5 h)-Y samples (Figure 1a),^[24] suggesting that these materials contain micro- and meso-/macroporosity typical of hierarchical zeolites,^[29] although corresponding NL-DFT pore size distributions only exhibited well-defined micropores ~0.8 nm (Figure 1b). Textural properties of Y zeolites and an Al-SBA-15 reference sample (Figure S4) are summarised in Table 1. Application of the *t*-plot model yielded a high micropore surface area and volume (V_{micro}) of 0.21 cm³.g⁻¹ for H–Y, while BJH analysis yielded a modest mesopore volume and surface area (S_{meso}) of 167 m².g⁻¹ likely due to intercrystallite voids.^[30] The total pore volume of 0.32 cm³.g⁻¹ for the parent H–Y is in good agreement with literature,^[25,27,31] which span 0.34–0.37 cm³.g⁻¹ total pore volume. Our micropore volume of 0.21 cm³.g⁻¹ for the parent H–Y is only slightly lower than values from these literature reports of 0.28–0.30 cm³.g⁻¹. For USY (CBV760), we determine a total pore volume of 0.35 cm³.g⁻¹ and micropore pore volume of 0.17 cm³.g⁻¹ respectively - values in good agreement with literature.^[32] BJH analysis of the treated zeolite evidenced an increase in mesopore volume associated with mesopores spanning ~2.5–10 nm (Figure S5). Dealumination by nitric acid washing, a mild treatment, induced a modest decrease in microporosity and concomitant increase in mesoporosity, resulting in minimal change in the hierarchy factor (HF, a measure of the relative micro- and mesoporosity) for DA(HNO₃0.5 h)-Y. Commercial USY closely resembled the DA(HNO₃0.5 h)-Y sample, whereas Al-SBA-15 was predominantly mesoporous as anticipated from templating of the parent SBA-15. Although the

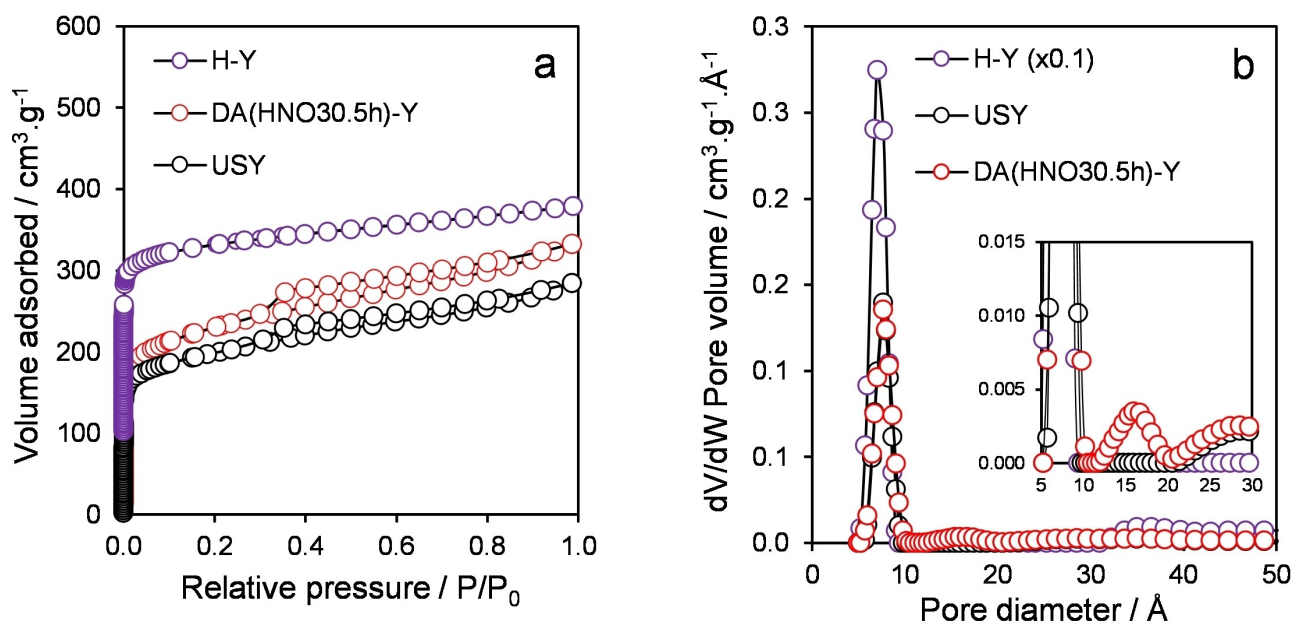


Figure 1. (a) Ar adsorption-desorption isotherms (H–Y offset by $200 \text{ cm}^3 \cdot \text{g}^{-1}$ for clarity) and (b) corresponding NLDFT pore size distributions of Y zeolites (inset: magnification highlighting well-defined mesopores in DA(HNO_3 0.5 h)-Y).

Table 1. Textural properties of catalysts using Ar adsorption-desorption.

Sample	$S_{\text{micro}}^{[a]}/\text{m}^2 \cdot \text{g}^{-1}$	$S_{\text{ext}}^{[a]}/\text{m}^2 \cdot \text{g}^{-1}$	$V_{\text{micro}}^{[a]}/\text{cm}^3 \cdot \text{g}^{-1}$	$V_{\text{meso}}^{[c]}/\text{cm}^3 \cdot \text{g}^{-1}$	$V_{\text{pore}}^{[a]}/\text{cm}^3 \cdot \text{g}^{-1}$	$D_p^{[b]}/\text{nm}$	HF ^[d]
H < C → Y	489	167	0.21	0.11	0.32	0.80	0.17
DA(HNO_3 0.5 h)-Y	373	296	0.15	0.22	0.37	0.84	0.18
USY	351	226	0.17	0.18	0.35	0.83	0.19
Al-SBA-15	41	496	0.05	0.63	0.68	1.20	0.07

[a] t-plot method; [b] NL-DFT model (median pore width); [c] BJH adsorption between 1.7–300 nm width; [d] $\text{HF} = \left(\frac{V_{\text{micro}}}{V_{\text{pore}}} \right) \times \left(\frac{S_{\text{meso}}}{S_{\text{Tot}}} \right)$ where V_{micro} is the micropore volume ($\text{cm}^3 \cdot \text{g}^{-1}$), V_{pore} the total pore volume ($\text{cm}^3 \cdot \text{g}^{-1}$), S_{meso} the mesopore surface area ($\text{m}^2 \cdot \text{g}^{-1}$) and S_{Tot} the total surface area (Table S5).

median pore diameter, D_p (Table 1), was dominated by micropore contributions, DA(HNO_3 0.5 h)-Y exhibited a small but significant proportion of mesopores with median diameters $\sim 1.6 \text{ nm}$ (much larger than TIPB, see inset to Figure 1b) which are absent in H–Y and USY.

Powder XRD patterns show the crystalline structure of the parent H–Y zeolite, and USY and DA(HNO_3 0.5 h)-Y samples, closely resembled that of faujasite (Figure 2), consistent with the large micron-sized crystals observed by TEM and SEM (Figure S6–S7). However, nitric acid washing slightly decreased the faujasite unit cell (evidenced by a small shift of reflections to higher angle). HRTEM images of the parent H–Y zeolite reveal cubic particles with pore diameters of $\sim 1 \text{ nm}$ (Figure S6). Well-defined lattice fringes and sharp Fast Fourier Transform (FFT) images were observed for H–Y and DA(HNO_3 0.5 h)-Y samples. Minimal changes in particle morphology were apparent following nitric acid washing of the parent H–Y, with uniform platelets observed for both samples by SEM (Figure S7). Note we could not obtain selected area electron diffraction patterns due to the high instability of particles under the electron beam.

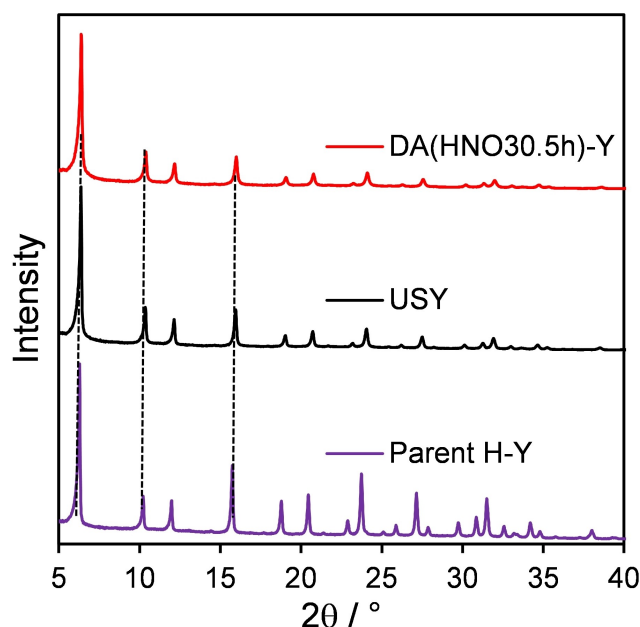


Figure 2. X-ray diffraction patterns of H–Y zeolites.

^{13}Al and ^{29}Si MAS NMR spectra were subsequently acquired to elucidate the Si and Al chemical environments (Figure 3). Aluminium present in a tetrahedral coordination is typically attributed to Al^{3+} ions introduced into a silica framework that are responsible for generating Brønsted acid sites,^[33] whereas that present in an octahedral coordination is attributed to extra-framework aluminium (often as amorphous alumina).^[34] The majority of Al in H–Y occupies tetrahedral sites, as indicated by sharp peaks between 40 and 70 ppm,^[35] with additional peaks at -5.2 and -8.2 characteristic of extra-framework Al.^[36] DA(HNO_3 0.5 h)-Y exhibits weaker peaks associated with tetrahedral Al, and a sharp, strong peak at -8.2 ppm indicative of well-defined extra-framework Al species such as crystalline alumina, which may lower the concentration of Brønsted acid sites. Corresponding ^{29}Si MAS NMR spectra of the parent H–Y zeolite showed peaks at -96 , -102 and -107 ppm assigned to Q4 (2Al), Q4 (1Al), and Q4 (0Al) species respectively, where Q4 represents a Si atom connected to four atoms in a tetrahedral coordination by bridging oxygen, and nAl indicates the number of Al atoms in the second coordination shell.^[35] Note that some reports assign peaks between -106 to -108 ppm to Si with one Al in the second coordination sphere.^[36] The intensities of Q4 (2Al) and Q4 (1Al) peaks are significantly weaker in DA(HNO_3 0.5 h)-Y, whereas a sharp, intense Si (0Al) line is retained at -108 ppm, both observations consistent with zeolite dealumination.^[37] Si:Al ratios (based on framework Al) calculated from the ^{29}Si directly polarized MAS NMR according to Eqn. 1 were ~ 3 and 13 for H–Y and DA(HNO_3 0.5 h)-Y, respectively:

$$\frac{\text{Si}}{\text{Al}} = \frac{\sum_{n=0}^4 I_{\text{Si}(n\text{Al})}}{\sum_{n=0}^4 0.25nI_{\text{Si}(n\text{Al})}} \quad (1)$$

Acid properties (concentration and strength) of the zeolites were also characterised by temperature programmed desorption of ammonia between 40 – 650 °C. All samples evidenced a single broad NH_3 desorption spanning 150 – 400 °C (Figure S8), which could be fitted with two peaks (mixed Gaussian:Lorentzian 30:70 functions) with maxima at 100 – 200 °C and 250 – 400 °C associated with weak and medium acid site strength,

respectively.^[24,38] Brønsted acidity arises from Al^{3+} cations isomorphically substituted for Si^{4+} cations in the silica framework, which are charge balanced by co-located protons within the pore network, present as bridging Si–O(H)–Al hydroxyls.^[39] Dealumination, which increases the framework Si:Al ratio, therefore lowers the BAS concentration. Lewis acidity may arise from oxygen vacancies in the zeolite framework or extra-framework aluminium oxides, which both result in under-coordinated metal cations (electron acceptor).^[40] The concentration of BAS in hierarchical zeolites was recently reported to decrease with increasing mesoporous or external surface area and LAS concentrations.^[41] Thermal pretreatment of the commercial H–Y zeolite (Si/Al=2.6) resulted in a slight dealumination of the high alumina sample. Evidence for this can be found in the observation of Lewis acidity (see Table 3) and a reduced micropore volume compared to literature (Table 1). Great care was taken to reduce this dealumination, but a compromise between decomposition of the ammonium forms and slight dealumination had to be found. In the present study, dealumination by acid washing lowered the total acid loading relative to the parent H–Y (Table 2), mirroring the loss of framework Al observed by MAS NMR.^[31b] Although the strongest acid sites in DA(HNO_3 0.5 h)-Y exhibited a slight increase in peak maximum desorption temperature relative to the parent H–Y (Table 2), acid washing lowered both the number and proportion of strong acid sites.

Zeolite acidity was further studied by a combination of in-situ FTIR of chemisorbed ammonia (Figure 4) and ex-situ chemisorbed pyridine DRIFT (Figure S11). Five distinct hydroxyl stretching vibrations are reported for zeolite Y.^[42] In this work, evacuated parent H–Y and the acid-washed zeolite exhibited bands at approximately 3744 cm^{-1} , 3660 cm^{-1} , 3630 cm^{-1} , 3602 cm^{-1} and 3560 cm^{-1} (Figure 4a and Figure S9) attributed to terminal silanols (Si–OH), non-acidic AlOH, Si–OH–Al groups in the zeolite supercages, OH groups influenced by extraframework Al species^[43] and sodalite cavities, respectively. For DA(HNO_3 0.5 h)-Y, the absence of a band at 3690 cm^{-1} (with a shoulder at 3660 cm^{-1}) evidences a lack of OH-groups connected to extraframework Al species within supercages, and hence the loss of extraframework material (which would

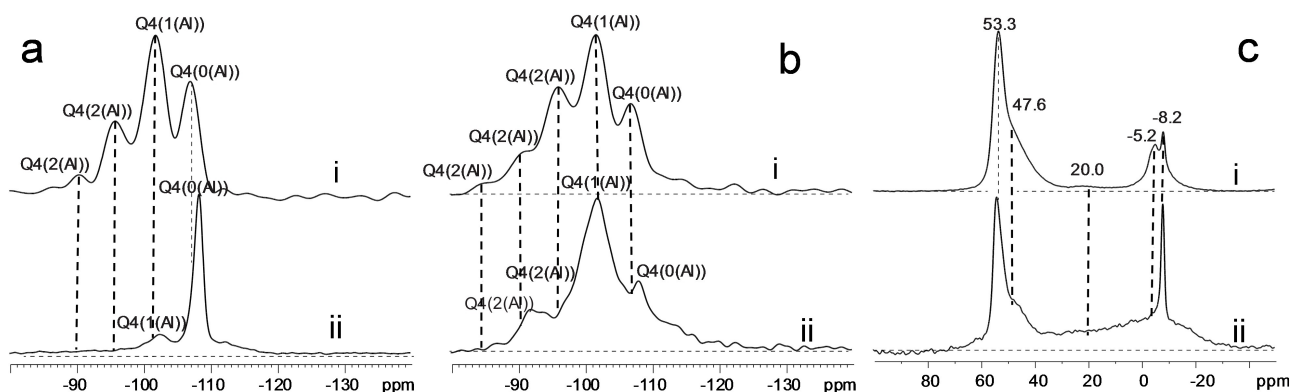


Figure 3. ^{29}Si and ^{27}Al solid-state nuclear magnetic resonance (NMR) using (a) ^{29}Si directly polarized MAS NMR 100 s recycle delay, 12 kHz MAS 768 scans, (b) ^{29}Si CPMAS NMR 2 s recycle delay, 2 ms CP contact 5 kHz MAS 8096 scans, and (c) ^{27}Al directly polarized NMR 0.2 s recycle delay, 8096 scans for (i) parent H–Y and (ii) DA(HNO_3 0.5 h)-Y.

Sample	Si:Al ratio ^[a]	Si:Al ^[b]	T _{max} (HTP) ^[c] /K	LTP ^[d] /mmol.g ⁻¹	HTP ^[d] /mmol.g ⁻¹	Total acid loading ^[d] /mmol.g ⁻¹
H-Y	3 (2.6 ^[e])	3	533	0.868	1.775	2.64
DA(HNO ₃ 0.5 h)-Y	18	13	592	0.481	0.325	0.81
USY	16		582	0.440	0.309	0.75
Al-SBA-15	10		656	0.320	0.400	0.72

[a] ICP-OES. [b] MAS NMR. [c] Maximum peak temperature from NH₃-TPD. [d] NH₃-TPD peak area calibrated against HZSM-5 (Si:Al = 15), LTP = low temperature peak (~100–200 °C) and HTP = high temperature peak (~250–400 °C). [e] Prior to 550 °C calcination.

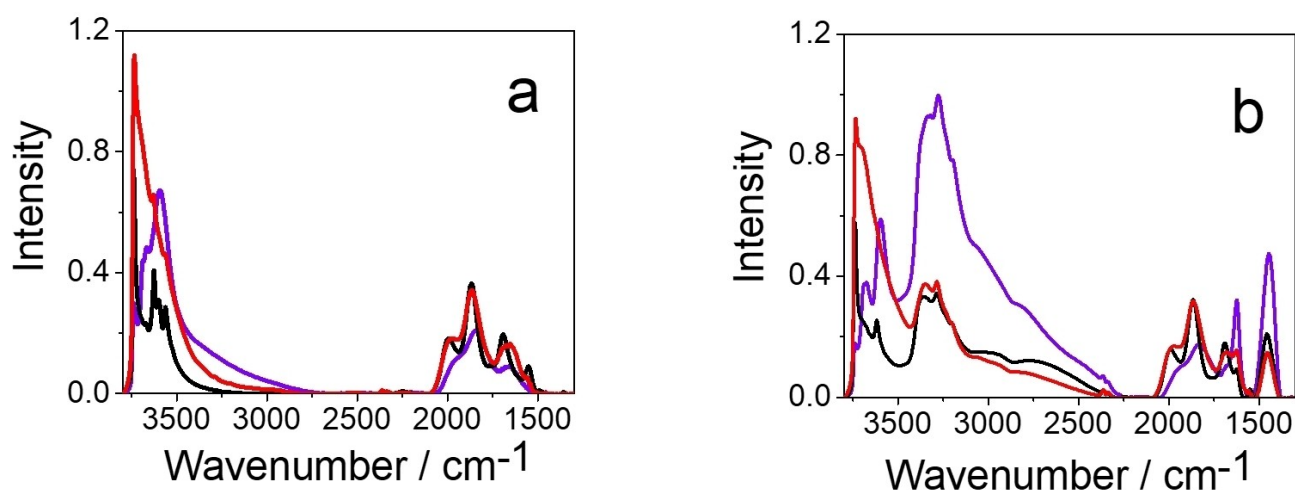


Figure 4. IR spectra normalised to lattice overtones of parent H-Y, USY and DA(HNO₃0.5 h)-Y (a) after evacuation at 10⁻⁷ mbar, (b) after 10 mbar NH₃ adsorption at 150 °C and subsequent evacuation. H-Y – violet, DA(HNO₃0.5 h)-Y – red, USY – black (spectra are normalized to the zeolite mass).

increase the BAS concentration/lower the LAS concentration).^[43] DA(HNO₃0.5 h)-Y and USY show similar hydroxyl spectra with an intense band (HF) from SiO₁HAl groups in the supercages at 3630 cm⁻¹ and a weaker band (LF) from SiO₃HAl groups in the small cavities at 3560 cm⁻¹.^[44] Perturbation of hydroxyl spectra by ammonia adsorption at 10 mbar and 150 °C and subsequent evacuation may reflect the adsorbate interaction with Brønsted acid sites (Figure 4b). Bands at 3744 cm⁻¹ and 3660 cm⁻¹ associated with terminal silanol and non-acidic AlOH species were unaffected by ammonia. In contrast, the HF and LF bands were strongly attenuated by adsorbed ammonia (possibly reflecting their Brønsted acidity (Figure S9)). All zeolites exhibited strong, broad bands between 3000–3500 cm⁻¹ due to N–H stretches, along with sharp bands at 1620 cm⁻¹ and 1445 cm⁻¹ which are reported as associated with the bending modes of

NH₃ and NH₄⁺ coordinated to LAS and BAS respectively.^[45] The NH₄⁺ deformation vibrations expected for Brønsted acid sites dominate the zeolites with bulk Si:Al ratios < 3, in accordance with literature.^[20b] This interpretation is supported by pyridine titration and quantification of the resultant DRIFT spectra to detect and quantify the Brønsted/Lewis character (Figure S11). The band at 1540 cm⁻¹ is commonly attributed to a pyridinium ion coordinated to Brønsted acid sites (B), with those at 1438 cm⁻¹ and 1580 cm⁻¹ attributed to molecular pyridine coordinated to Lewis acid sites (L), the 1488 cm⁻¹ band is observed from pyridine adsorbed over both Brønsted and Lewis acid sites (B + L).^[46]

Table 3 summarises the Brønsted and Lewis acid site loadings, obtained by scaling the total acid site loadings from NH₃ TPD and BAS:LAS ratio from pyridine DRIFTS. Ammonia

Sample	Brønsted:Lewis ratio ^[a]	Brønsted acid loading ^[b] /mmol.g ⁻¹	Lewis acid loading ^[b] /mmol.g ⁻¹
H < C → Y	2.45	1.56	0.64
USY	3.03	0.50	0.17
DA(HNO ₃ 0.5 h)-Y	3.32	0.57	0.17
Al-SBA-15	3.01	0.48	0.16

[a] Pyridine DRIFTS, [b] NH₃-TPD (BAS or LAS = total acid loading × proportion of BAS or LAS from pyridine DRIFTS).

adsorption over Al-SBA-15 resulted in similar spectral changes (Figure S10), with sharp bands appearing at 1620 cm^{-1} and 1445 cm^{-1} due to LAS and BAS, in addition to an intense terminal silanol band at 3744 cm^{-1} .

Time domain NMR was employed to confirm hierarchical pore structure connectivity within dealuminated materials. Figure 5 provides a comparison of $T_1 - T_2$ correlation data for unrestricted water, and for water interacting with both the parent zeolite H-Y and the dealuminated DA(HNO₃0.5 h)-Y zeolite. Relaxation times for unrestricted water are on the order of several seconds, as expected for bulk liquids,^[47] with $\langle T_1 \rangle \approx 3.1\text{ s}$ and $\langle T_2 \rangle \approx 2.7\text{ s}$, wherein angular brackets indicate the modal relaxation times of the distribution (for mathematical derivations see Experimental Eqns. 2–3). For water interacting with zeolite powders, these relaxation times are expected to decrease (corresponding with enhanced nuclear spin relaxation rates $T_{1,2}^{-1}$) as a result of confinement within the zeolite pore networks. Such relaxation dynamics are well described by the simple expression $T_{1,2}^{-1} \approx \rho_{1,2} d^{-1}$, where $T_{1,2}^{-1}$ are the experimentally observed relaxation rates and d is the size of the confining pore structure; $\rho_{1,2}$ are the surface relaxivities of the porous material and describe enhanced rates of nuclear spin relaxation by species at the solid-fluid interface. In the present work such enhancement occurs due to a reduction in molecular dynamics due to adsorption at the pore surface,^[48] dipolar interactions with surface bound ¹H spins in the form of Brønsted acid sites,^[49] and through ¹H exchange with those sites.^[50] Importantly, these surface relaxivities act as an approximate scaling factor between observed relaxation and pore size, such that materials exhibiting smaller pores will present shorter NMR relaxation times. A single relaxation population is observed for water interacting with zeolite H-Y, indicative of rapid exchange

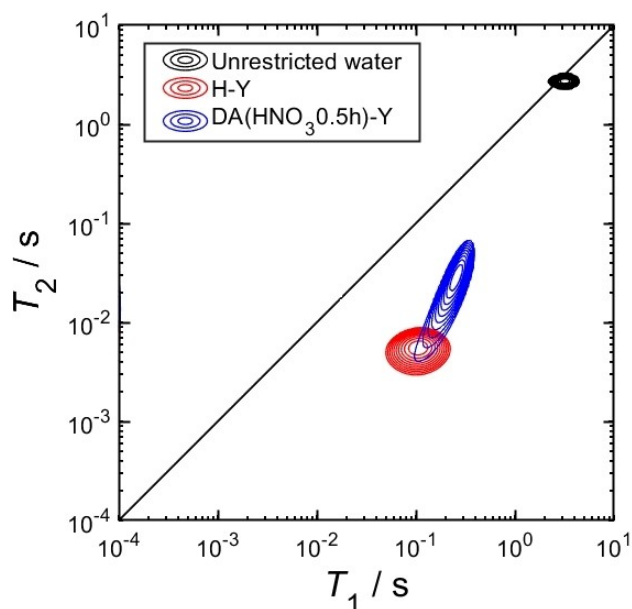


Figure 5. ¹H $T_1 - T_2$ correlation data for bulk (unrestricted) water, together with water interacting with zeolite H-Y and with DA(HNO₃0.5 h)-Y. Correlation peaks indicated the relative probability of each system exhibiting a given combination of T_1 and T_2 relaxation time constants, while the solid diagonal line indicates the $T_1 = T_2$ parity ratio.

between water within the zeolite micropores and within the interparticle space (bulk media), such that the observed relaxation times must correspond with a weighted average of these two water populations. The short relaxation times observed ($\langle T_1 \rangle \approx 0.1\text{ s}$ and $\langle T_2 \rangle \approx 0.005\text{ s}$) suggest these data are dominated by the most rapid relaxation process present, corresponding with water confined within the H-Y micropores. A single population is also observed for water interacting with DA(HNO₃0.5 h)-Y, in turn suggesting rapid exchange (and hence connectivity) between pore structures within the material (as well as with the interparticle space), while the increase in modal relaxation times ($\langle T_1 \rangle \approx 0.25\text{ s}$ and $\langle T_2 \rangle \approx 0.026\text{ s}$), relative to zeolite H-Y, indicates that imbibed water experiences pore structures of increased size within this material. While care must be taken in interpreting the shape of NMR relaxation distributions,^[51,52] elongation of this relaxation distribution away from the zeolite H-Y data indicates enhanced pore size heterogeneity within this dealuminated material, relative to zeolite H-Y, supporting the existence of a connected, hierarchical pore structure.

Figure 6a shows PFG NMR diffusion data for water within zeolite H-Y. A single diffusion population is observed, as characterised by a mono-exponential data decay. The solid line indicates a fit to Eqns. 4 and 5, yielding a self-diffusion coefficient of $D = 1.40 \pm 0.02 \times 10^{-9}\text{ m}^2\text{ s}^{-1}$. The associated root mean square displacement (RMSD) = $\sqrt{2\Delta D} \approx 17\text{ }\mu\text{m}$; as this length scale is significantly larger than the associated zeolite crystallites (Figure S6–S7) the observed diffusion behaviour is interpreted as a “long-range” diffusivity,^[53] characterised by a weighted average of water diffusivities within both the H-Y micropores and within the interparticle voids. Figure 6b shows PFG NMR diffusion data for water in DA(HNO₃0.5 h)-Y. Here, two separate diffusion populations are readily identified, corresponding with a biexponential data decay. The solid line indicates a fit to Eqns. 5 and 6; this fit yields a large population (>98% of the observed NMR signal) characterised by $D_1 = 1.64 \pm 0.02 \times 10^{-9}\text{ m}^2\text{ s}^{-1}$, together with a small population characterised by $D_2 = 3 \pm 0.5 \times 10^{-10}\text{ m}^2\text{ s}^{-1}$. The large, more rapidly diffusing component is again interpreted as long-range diffusion across both the zeolite (micro- and mesopore) structure and interparticle voids, and contrasts with the diffusive characteristics of water in H-Y.

Given the identical particle structure (and hence packing) of the two materials investigated, the increased long-range diffusivity of water within DA(HNO₃0.5 h)-Y, relative to H-Y, indicates a decrease in diffusive restrictions within the zeolite upon dealumination, consistent with the incorporation of mesoporosity within the material pore structure. This behaviour may be quantified via calculation of the effective tortuosity D_0/D ,^[54] where $D_0 = 2.48 \pm 0.01 \times 10^{-9}\text{ m}^2\text{ s}^{-1}$ (data not shown) is the self-diffusion coefficient of unrestricted water at 28 °C, and wherein values tend towards 1 as a function of decreasing diffusive restriction: we obtain $D_0/D = 1.77 \pm 0.01$ for H-Y and $D_0/D = 1.51 \pm 0.01$ for DA(HNO₃0.5 h)-Y. Finally, given the decrease in accessible micropore volume and surface area upon treatment of the parent zeolite with nitric acid (Table 1), we conjecture that the very small diffusive population ($\sim 1\%$ of

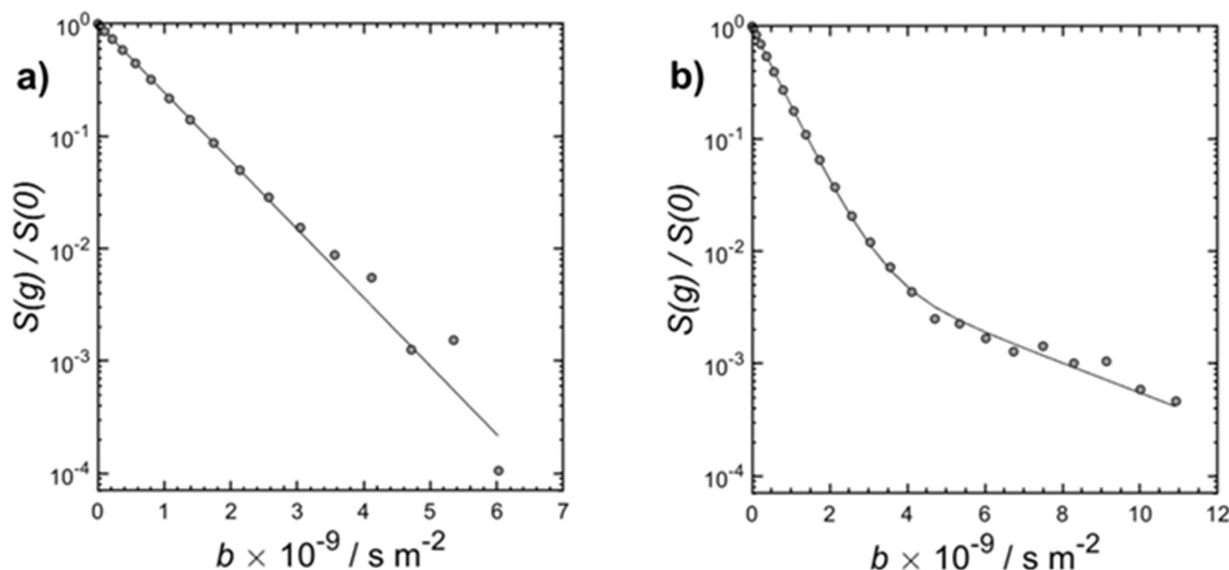


Figure 6. PGSTE data for water interacting with a) zeolite H-Y and b) dealuminated zeolite DA(HNO₃ 0.5 h)-Y. The one-component fit in panel a) utilised equation (4), while the two-component fit in panel b) utilised equation (6).

the observed NMR signal) characterised by D_2 may arise from a highly restricted water population ($D_0/D = 8.14 \pm 0.18$) resulting from micropore blocking during mesopore creation. Extensive additional diffusion measurements will be required to fully identify the source of this slowly diffusion population, and will be the subject of future work.

Catalytic cracking of 1,3,5-TIPB

The catalytic performance of the preceding zeolites and Al-SBA-15 was subsequently explored for the vapour phase cracking of

1,3,5-TIPB at 350 °C (Figure 7 and Table 4) and modest conversions under integral reactor operation. Catalytic cracking of 1,3,5-triisopropylbenzene (TIPB) is widely reported as a probe reaction to evaluate the acidity and active site accessibility of microporous and hierarchical zeolites.^[25,31a] TIPB is a symmetric molecule with a kinetic diameter of ~ 0.94 nm,^[55] larger than the 12-ring pore diameter of a microporous Y zeolite (micropore diameter ~ 0.74 nm), and hence can only react at acid sites on the external (low) surface of microporous particles or within mesopores (which facilitate access to in-pore active sites).^[56] The product of this extra-pore or mesopore chemistry, 1,3-diisopropylbenzene (DIPB) with a kinetic diameter of 0.84 nm,^[57]

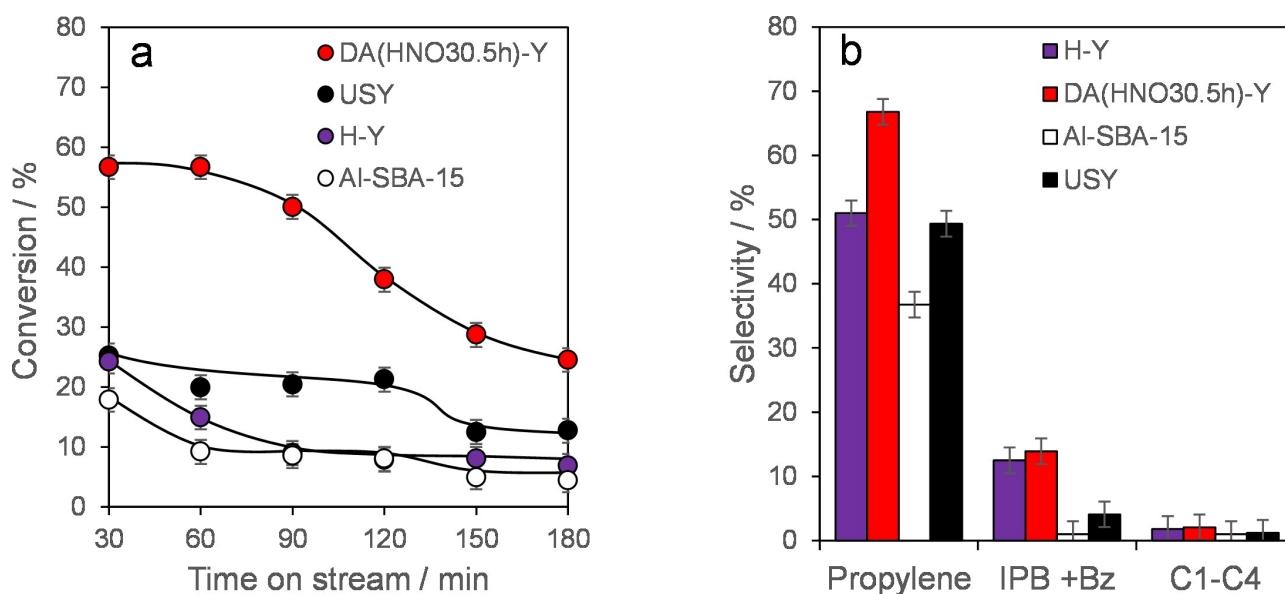


Figure 7. (a) Conversion of 1,3,5-TIPB and (b) product selectivity at 120 min TOS for Y zeolites and Al-SBA-15 catalysts. Reaction conditions: $T = 350$ °C, $P = 1$ bar, $WHSV = 0.7$ min⁻¹.

Table 4. Catalytic performance of solid acid catalysts for 1,3,5-TIPB cracking in a continuous-flow reactor.^[a]

Sample	Al-SBA-15	DA(HNO ₃ 0.5 h)-Y	HY	USY
V _{micro} ^[b] (cm ³ .g ⁻¹)	0.05	0.15	0.21	0.17
S _{ext} ^[b] (cm ² .g ⁻¹)	496	296	167	226
Total acid conc. ^[d] (mmol/g _{cat})	0.72	0.8	2.64	0.82
X _{TIPB} (%) ^[d]	4	25	7	13
Y _{DIPB's} (%) ^[d]	2.50	3.36	4.57	3.54
Y _{Bz+IPB} (%) ^[d]	0.08	2.46	0.37	0.49
Y _{methane} (%) ^[d]	0.00	0.04	0.00	0.00
Y _{ethene} (%) ^[d]	0.00	0.01	0.01	0.00
Y _{ethane} (%) ^[d]	0.00	0.00	0.00	0.00
Y _{propylene} (%) ^[d]	1.50	18.56	1.91	8.65
Y _{propane} (%) ^[d]	0.01	0.04	0.00	0.00
Y _{butene} (%) ^[d]	0.02	0.03	0.01	0.03
Carbon balance ^[e] (%)	100	100	99.3	99.4
Specific activity _{TIPB} ^[f] (10 ² mol _{TIPB} .g ⁻¹ _{cat} .s ⁻¹)	0.04	0.25	0.07	0.13
TOF _{cracking} ^[g] (s ⁻¹)	0.8	4.4	0.4	2.5

[a] Reaction conditions: T (350 °C), WHSV (0.7 min⁻¹), TIPB (0.07 g.min⁻¹), catalyst (0.1 g), P (1 bar), N₂ flow rate (50 mL.min⁻¹). [b] t-plot method. [c] NH₃-TPD. [d] Values at 180 min TOS. [e] Carbon balance at 180 min TOS. [f] Specific activity at 180 min TOS. [g] Rate of TIPB conversion at 180 min TOS normalised to Brønsted acid loading at conversion levels < 10% where conversion was linear with TOS.

is also too large to access micropores in unmodified H–Y for further cracking reactions. In contrast, acid-etched H–Y catalysts possessing mesopores should facilitate in-pore cracking of TIPB and DIPB, *provided such mesopores contain a sufficient number and strength of acid sites*. Deep cracking of 1,3,5-TIPB is a term coined by Hosseinpour et al. to describe the formation of cumene (and benzene) arising from the successive dealkylation of DIPB (and cumene) to benzene and propylene.^[58,59] Note that a high propylene yield is not indicative of deep cracking as it may simply reflect high 1,3,5-TIPB conversion to diisopropylbenzene, whereas cumene and benzene yields are direct measures of deep cracking. Relationships between deep cracking and mesoporosity are previously discussed for zeolites.^[14,60] Aghakhani et al showed that composites of amorphous aluminosilicate (ASA) and Y zeolite facilitated TIPB pre-cracking during diffusion through a mesoporous ASA shell, with resulting DIPB isomers cracked to cumene and benzene over acid sites in the zeolite core.^[55] Mesopores arising from acid-base treatments are also reported to increase the accessibility of strong Brønsted acid sites in ZSM-5, promoting TIPB conversion to deep cracking products (combined cumene and benzene selectivity of 23% versus 18% for untreated ZSM-5). A recent report by Trujillo and co-workers suggested that benzene selectivity is insensitive to zeolite Y mesoporosity,^[61] but assumed that DIPB can access zeolite micropores, which is not possible for any of the Y zeolites in this work (Table 1, D_p ≤ 0.84 nm). Cumene and benzene yield (not selectivity) are thus a valuable indicator of *the number of strong acid sites accessible to DIPB*, and to a lesser extent accessible to cumene (kinetic diameter of 0.68 nm), and hence the propensity for deep cracking.

Considering Figure 7, the parent H–Y exhibited a low initial 1,3,5-TIPB conversion of ~25% which decreased monotonically to < 10% after 180 min TOS, similar to values reached by Al-SBA-15 and USY. In contrast, dealumination by nitric acid washing significantly enhanced activity, with an initial 1,3,5-TIPB conversion of 58% decreasing to 25% after 180 min. DA-(HNO₃0.5 h)-Y also exhibited the highest selectivity to deep cracking products after 120 min TOS, with the parent H–Y more selective than its more active USY counterpart. Al-SBA-15 was essentially inert for deep cracking as previously reported.^[62] Specific activities after 180 min TOS followed the sequence DA(HNO₃0.5 h)-Y > USY ≫ H–Y > Al-SBA-15, and are uncorrelated with total acid site loading, acid strength or hierarchy factor. The only logical conclusion is that acid sites located in ~1.6 nm mesopores present in DA(HNO₃0.5 h)-Y are disproportionately active for TIPB pre-cracking to DIPB. Despite a low acid loading and modest proportion of strong acid sites, DA(HNO₃0.5 h)-Y was also the most active catalyst for deep cracking, with a combined cumene (IPB) and benzene yield approximately five times greater than any other catalyst. We postulate that diffusion of reactively-formed DIPB and cumene, produced in the mesopores of DA(HNO₃0.5 h)-Y, to additional active sites within interconnected micropores, is more rapid than diffusion from the external surface of H–Y nanocrystals into micropores. In other words, mesopores reduce the diffusion path length for pre-cracking products to access microporous acid sites for deep cracking reactions. Acid character was also an important factor in TIPB pre-cracking, with corresponding specific activities and turnover frequencies (TOFs, per BAS from NH₃-TPD determined for differential operation < 10% conversion at a WHSV of 1.5 min⁻¹) directly proportional to the Brønsted:Lewis ratio

(determined from NH_3 FTIR data, Table 3) as seen in Figure 8. Dealumination with nitric acid was the most effective method for enhancing Brønsted acidity, previously conjectured as a prerequisite for DIPB dealkylation.^[62] Note that a Na–Y analogue of the parent H–Y was completely inert towards 1,3,5-TIPB ($X_{\text{TIPB}} = 0\%$) highlighting the importance of solid acid sites.^[63] In all cases, carbon mass balances were almost 100%. Secondary mesoporosity in the DA(HNO_3 , 0.5 h)-Y catalyst arising from dealumination may also mitigate deactivation by coke deposition accounting for the significant rate of 1,3,5-TIPB conversion (> 20%) maintained after 180 min TOS.

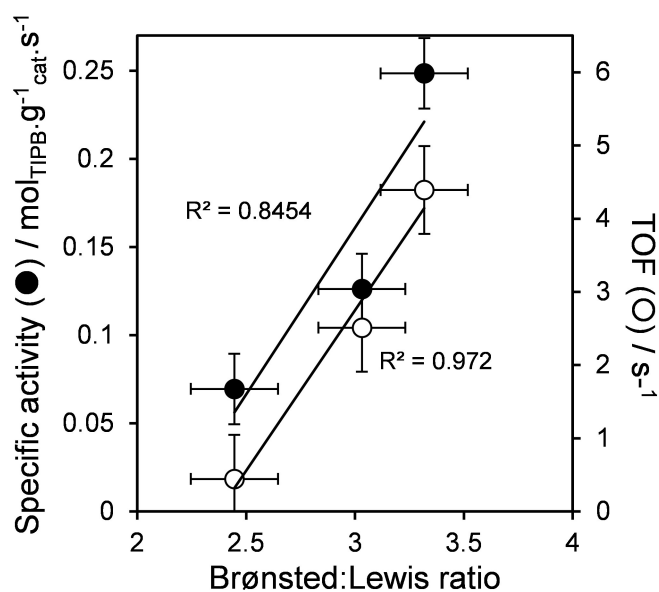


Figure 8. Dependence of specific activity and TOF for 1,3,5-TIPB cracking on Brønsted:Lewis ratio of Y zeolites. TOFs were determined under differential conditions at < 10% conversion.

Catalytic cracking of LDPE

The performance of Y zeolites was for the catalytic cracking of a real plastic feedstock, virgin LDPE dissolved in toluene, was also investigated in the same continuous fixed-bed flow reactor. Control reactions using pure toluene evidenced negligible solvent conversion or alkyl aromatic products from toluene disproportionation (Table S6), with only trace benzene, xylenes and ethylbenzene observed.^[64]

DA(HNO_3 , 0.5 h)-Y and H–Y were the most active catalysts, achieving 99% and 81% LDPE conversion respectively (Figure 9), with Al-SBA-15 significantly less active. A Lewis acidic Na–Y counterpart (not shown) of the parent H–Y zeolite was almost inactive (6% conversion).^[65] In contrast to 1,3,5-TIPB, the conversion of LDPE was independent of the Brønsted:Lewis ratio, and also the total acid loading, and mesopore volume and only weakly correlated with hierarchy factor (Figure S12a). However, within the family of Y zeolites, LDPE conversion was directly proportional to the total pore volume (Figure S12b), indicating that textural properties were more important than acidity for depolymerisation. These observations are consistent with reports that LDPE degradation can be initiated by either LAS or BAS, involving respective hydride abstraction or protonation of a C–C bond in the transition state,^[66] and hence a lack of preference for Brønsted or Lewis acid character. Activated polyethylene molecules subsequently undergo successive β -scissions to form lower molecular weight fragments.^[67] The importance of hierarchical porosity in achieving high LDPE conversion is expected; accessibility of bulky polymer chains to in-pore active sites is likely rate-limiting for microporous (H–Y) zeolites. Unlike the behaviour of lamellar and pillared ZSM-5 zeolites, we found no correlation between LDPE conversion and the concentration of BAS or mesopore/external surface area.^[68] Although Al-SBA-15 possesses a higher porosity than any Y zeolite, the higher acid strength of the former (peak maximum

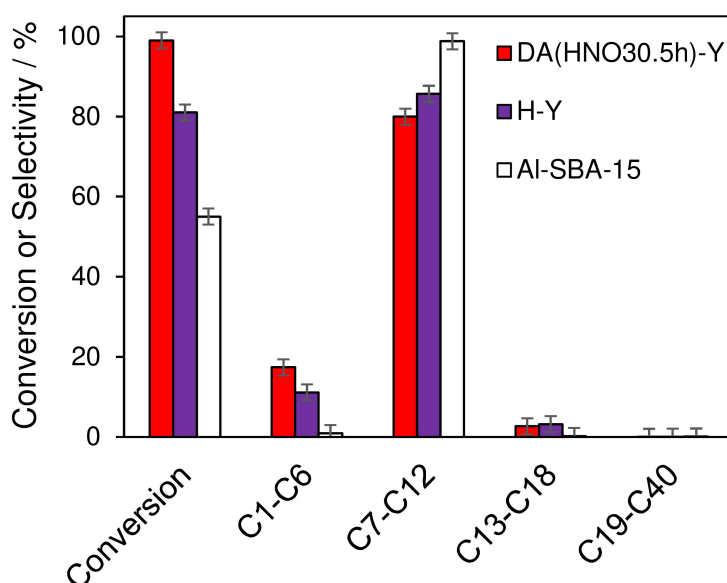


Figure 9. Product evolution during LDPE cracking over (DA(HNO_3 , 0.5 h)-Y, H–Y, and Al-SBA-15 at 120 mins (Reaction conditions: $T = 380^\circ\text{C}$, TOS = 2 h, WHSV = 222 h^{-1}).

desorption temperature ~656 K versus 530–590 K, Table 2) could induce pore-blockage by strongly adsorbed carbon residues, accounting for its modest conversion.

In all cases, the major products (<70 wt.%) were C7–C12 hydrocarbons, predominantly xylenes, ethylbenzene and methylcyclohexane (Table S7), with a small proportion of <C6 hydrocarbons (benzene and aliphatic alkanes and alkenes), and trace heavier hydrocarbons (4-methyl-octane and 2,2-dimethyl-heptane). The combined yield of benzene and xylene isomers was 33% greater for the hierarchical mesoporous DA(HNO₃0.5 h)-Y than the parent H–Y after 120 min TOS. High selectivity to liquid hydrocarbons is beneficial for fuel applications which require aromatic and alicyclic feedstocks amenable to ring-opening/hydrogenation.^[69] The H–Y catalyst delivered slightly higher selectivity to C7–C12 cracking products than their dealuminated counterpart, with the latter slightly more selective for deep cracking to <C6 products (Figure S13). The nitric acid washed catalyst was the most selective to C₃, C₄, and C₄= products, whose formation requires Brønsted acid sites driving carbocation chemistry and end-chain cracking of the polymer backbone. In contrast, the low activity, Lewis acidic Na–Y catalyst promoted a random-chain cracking mechanism with increased selectivity to middle distillates (C₁₃–C₂₂, not shown).

Ammonia titrates acid sites present within micro- and mesopores, and those on the external surface of zeolite crystals. Although acid sites within micropores are inaccessible to 1,3,5-TIPB and the virgin LDPE, this is not the case for their cracking products (e.g. DIPB and ethylene oligomers) whose molecular dimensions are sufficiently small to access micropores. Ammonia does therefore titrate acid sites which could catalyse secondary cracking steps responsible for cumene and benzene production from TIPB and e.g. xylenes, ethylbenzene, benzene and aliphatic alkanes/alkenes from LDPE. The correlation between TOFs (obtained by normalising catalyst activity to acid site loadings titrated by ammonia) and Brønsted:Lewis acid character determined by DRIFTS of chemisorbed pyridine strongly supports the postulate that all acid sites contribute to molecular cracking.

Conclusions

The impact of chemical pretreatments on the physicochemical properties of H–Y zeolite was investigated to elucidate the importance of structure and acidity on the thermal cracking of 1,3,5-TIPB and pristine LDPE. Dealumination by nitric acid washing (DA(HNO₃0.5 h)-Y) introduced mesoporosity without compromising surface area, but decreased the total acid loading (from 2.64 mmol.g⁻¹ to 0.81 mmol.g⁻¹). Dealumination of the H–Y zeolite by nitric acid washing increased catalytic activity ten-fold (TOF_{cracking} = 4.4 s⁻¹) for 1,3,5-TIPB cracking in a continuous fixed-bed flow reactor at 350 °C and a WHSV of 0.7 min⁻¹, and afforded a five-fold increase in the yield of deep cracking products (cumene and benzene), significantly outperforming commercial USY. The superior performance of DA(HNO₃0.5 h)-Y is attributed to improved in-pore acid site

accessibility to the bulky reactant, enhanced diffusion of reactive-intermediates to acid sites within micropores, and an increase in Brønsted acidity which suggests that C–C scission occurs via a carbonium ion pathway. LDPE cracking in the same reactor at 380 °C also exhibited significant promotion over DA(HNO₃0.5 h)-Y versus H–Y, affording 99% LDPE conversion and 98% selectivity to C₁–C₁₂ hydrocarbons (predominantly C_{7–12} in the gasoline range). Introduction of mesoporosity into H–Y zeolite is beneficial for the deep cracking of aromatics and branched homopolymers for chemical recycling and/or transport fuels production, but must be balanced against structural collapse and loss of desirable acidic properties. Future studies will explore methods to introduce ordered mesopores (to accelerate mass transport) without loss of acid loading to enhance activity.

Experimental Section

Catalyst preparation

Two commercial Y zeolites were provided by Zeolyst International in the ammonium form as starting materials for post-synthetic modification (CBV300, NH₄ form with nominal Si:Al atomic ratios of 2.6 and 6), alongside a NaY zeolite reference material (CBV100, nominal Si:Al = 2.6) and USY (CBV760). Post-synthetic modification was performed via dealumination by HNO₃ using 100 mL solutions with a zeolite concentration of 67 g.L⁻¹ under magnetic stirring in a round-bottomed flask equipped with a reflux condenser. In a typical experiment, the zeolite sample was added to a vigorously stirred solution of the desired chemical agent for a fixed time: 0.3 M HNO₃ at 100 °C for 0.5 h. The reaction was quenched in an ice bath and the resulting solids centrifuged, washed with deionised water, and dried overnight at 80 °C, followed by washing, ion-exchange and calcination at 550 °C for 5 h (ramp rate 2 °C.min⁻¹).

The parent (protonated) Y zeolite and the sample prepared by HNO₃ dealumination were designated H–Y and DA(HNO₃0.5 h)-Y (Table S1) respectively. The Si:Al ratio is specified for all samples, e.g. HY-3 indicates the parent HY zeolite with Si:Al = 3. Protonic forms of all zeolites were prepared by three consecutive ion exchanges in 0.5 M NH₄NO₃ (50 °C, 5 h); samples were then dried, pressed, calcined in air at 500 °C for 6 h, and sieved to a 250–600 μm size fraction. Na⁺-forms of zeolites (without an NH₄⁺ ion-exchange) were used as Lewis acid reference materials.

While great care has been taken to avoid steaming and dealumination (calcination ramp rate 2 °C.min⁻¹ to 550 °C) for the parent zeolite with Si/Al = 2.6 some dealumination occurred (*vide infra*). These conditions were an optimum between minimising dealumination and ensuring complete conversion of the ammonium to the proton form.

SBA-15 was synthesised according to the literature^[70] with post-synthesis dealumination^[71] to produce Al-SBA-15. Briefly, 10 g of calcined SBA-15 was hydrolysed in 100 mL of AlCl₃·6H₂O (0.085 M) and 100 mL of aqueous tetramethylammonium hydroxide (TMAOH, 10 wt.% in water, Fluka) at 80 °C for 2 h. The resulting mixture was filtered, washed until pH neutral, and dried at 100 °C overnight, prior to annealing in flowing N₂ (150 mL.min⁻¹) at 600 °C for 5 h (ramp rate 2 °C.min⁻¹) to remove residual inorganic species. A pure SBA-15 was also prepared as a non-acidic analogue.

Catalyst characterisation

The Si:Al atomic ratios of zeolites were determined using a Varian Radial 715-ES Inductively Coupled Plasma-Optical Emission Spectrometer equipped with a Sturman-Masters spray chamber, quartz torch, and SPS 3 autosampler. Sample digestion was performed in a Milestone Start D microwave digestion system using a mixture of 4.5 mL HNO₃ (65%), 4.5 mL HCl (37%), and 3 mL HBF₄ (50%).^[72] Powder X-ray diffraction (XRD) patterns were acquired using a Malvern Panalytical X'pert diffractometer in Bragg-Brentano geometry using Cu K_{α1} radiation ($\lambda=0.1541$ nm) and K_{α2} radiation ($\lambda=0.1544$ nm) and without monochromator filtering. Diffractograms were recorded for $2\theta=5-90^\circ$ with a step size of 0.013° and dwell time of 3 s per step and an X-ray voltage and current of 40 kV and 40 mA. Phase identification was performed using X'pert Highscore software. Si and Al concentrations were determined by scanning electron microscopy (SEM) using a Zeiss Sigma VP electron microscopy for imaging at 30 kV and energy dispersive X-ray (EDX) elemental mapping. Transmission electron microscopy (TEM) imaging and EDX elemental mapping was conducted on a JEOL TEM 2100 microscope operated at 200 kV. Characterization of crystal nanostructures was performed by selected area electron diffraction (SAED). Samples were suspended in ethanol (99.9%) and ground to fine particles, ultrasonicated for 15 min and then drop-cast on holey-carbon film grids (ProSciTech, Australia).

Ammonia temperature-programmed desorption (NH₃-TPD) was undertaken in a bespoke instrument comprising a rotary pump and Pfeiffer HiCube 80 Eco turbopump connected to a quartz sample chamber, equipped with pressure gauges, a dosing valve, a programmable tube furnace, and gas analysis by a Pfeiffer Prisma QME 200 mass spectrometer as described elsewhere.^[73] 100 mg sample was heated in vacuo to 500 °C (ramp rate 10 °C.min⁻¹) for 60 min, then cooled to 150 °C prior to NH₃ adsorption at 10 mbar (sufficient to saturate all acid sites). An NH₃ TPD was then performed from 40 °C–650 °C (ramp rate 5 °C.min⁻¹) and the $m/z=16$ amu signal analysed to quantify the acid concentration relative to a HZSM-5(15) reference (~1 mmol.g⁻¹). Textural properties were determined by N₂ and Ar physisorption at -196 °C using a Micromeritics Tristar surface area analyser and Micromeritics 3Flex automated gas adsorption analyser. Samples (120–150 mg) were loaded into a quartz tube and degassed on a Micromeritics Smart VacPrep at 90 °C for 60 min and subsequently at 240 °C for 4 h. AR-NLDFT was used to derive the pore size distribution from the adsorption branch of the isotherm, assuming a cylindrical pore model for Ar on H-zeolite. The t-plot method was used to calculate the micro- and mesoporosity surface areas in the pressure range (p/p_0) of 0.08 to 0.27. The mesopore size distribution was obtained by the Barrett-Joyner-Halenda (BJH) model applied to the adsorption branch of the isotherm. Fourier Transform infrared (FTIR) spectra were collected using a Bruker Tensor27 FTIR spectrophotometer on self-supporting wafers (19 mg.cm⁻¹) mounted in a bespoke cell fitted with KBr windows. The cell was attached to a high vacuum line for in-situ thermal treatments and adsorption of probe molecules. Wafers were heated to 500 °C (ramp rate 10 °C.min⁻¹) for 1 h at 10⁻⁷ mbar to remove any adsorbates, then cooled to 150 °C (at 10 °C.min⁻¹). Ammonia adsorption was subsequently performed from 10⁻⁷–10 mbar during spectral acquisition at 4 cm⁻¹ resolution. Brønsted and Lewis acid site loadings were quantitatively determined from the intensities of NH₄⁺ and NH₃L bands arising from ammonia adsorption, using extinction coefficients (ϵ) of 0.11 and 0.026 cm²μmol⁻¹ for NH₄⁺ (Brønsted), NH₃-L (Lewis) acid bands and $\epsilon_{(\text{Brønsted})}=1.67$, $\epsilon_{(\text{Lewis})}=2.22$ cm²μmol⁻¹ for pyridine DRIFT spectra bands at 1545 cm⁻¹ and 1460 cm⁻¹ respectively.^[74] Ex-situ pyridine adsorption was performed by dropping approximately 100 μL of pyridine (99.8%, Sigma-Aldrich) onto 20 mg of sample. Excess physisorbed pyridine was removed in vacuo at 30 °C overnight prior

to recording the Diffuse Reflectance Infrared Fourier Transform Spectroscopy (DRIFT) spectra on a PerkinElmer FT-IR Spectrometer.

Solid-state nuclear magnetic resonance (NMR) spectra were acquired on a Bruker Biospin Avance III 300 MHz spectrometer at The University of New South Wales, using a wider bore 7 Tesla superconducting magnet, operated at 59.5 MHz and 300 MHz for ²⁹Si and ¹H nuclei respectively. Approximately 100 mg of sample was packed in 4 mm diameter zirconia rotors fitted with Kel-f® caps and spun in a double resonance H–X probehead at 12 kHz at the magic angle. The ²⁹Si 90° radio frequency pulse length was optimized to 5 μs. ²⁹Si MAS-NMR spectra were acquired using a Hahn echo sequence. Free induction decays of 20 ms were acquired with recycle delays of 100 s, and up to 2 k signal transients co-added for sufficient signal to noise. The Spinal64 scheme was used for ¹H decoupling with a wield strength of 71.5 kHz. ²⁹Si[¹H] cross-polarisation with magic angle spinning (CPMAS) experiments were acquired at 5 kHz, 2 s recycled delays, 5 ms to 10 ms of acquisition time, 2 ms of Hartman Hahn contact time for signal transfer from ¹H to ²⁹Si, and up to 8 k signal transients co-added to achieve a sufficient signal:noise level. ²⁹Si chemical shifts were referenced to tetramethylsilane using the kaolinite peak at -92.0 ppm as a secondary reference. ²⁷Al NMR experiments were acquired using a Bruker Biospin Avance III 700 MHz spectrometer, with a 16.4 Tesla superconducting magnet, operated at 182.5 MHz. Approximately 10 mg of samples were packed into 2.5 mm diameter zirconia rotors fitted with Vespel® capes and spun in a triple resonance H/X/Y probehead at 20 kHz. Spectra were acquired with a hard 2.2 μs pulse with 0.2 s recycle delay and up to 8k signal transients for sufficient signal to noise. ²⁷Al spectra were referenced to a 1 M Al(NO₃)₃ solution using the kaolin peak at -2.4 ppm as a secondary reference.

Time domain NMR data were acquired using a benchtop Magritek Spinsolve Diffusion spectrometer (Magritek, New Zealand) equipped with a cylindrical 1 T Halbach magnet array (providing a ¹H NMR frequency of 43 MHz) and a gradient coil capable of producing pulsed magnetic field gradients up to 1 T m⁻¹. Samples were prepared by loading standard 5 mm NMR tubes (Bruker BioSpin) with zeolite powder up to a height of ~5 cm, so as to fill the active region of the magnet bore; two samples were prepared, comprising the parent zeolite H–Y and nitric acid dealuminated Y (DA(HNO₃0.5 h-Y)), respectively. Each powder was soaked in excess deionised water for at least 72 hours under ambient condition, with the dynamics of the imbibed water interrogated using ¹H NMR relaxation and diffusion measurements. All time domain NMR measurements were performed at the default spectrometer temperature of 28 °C, with each sample placed within the magnet bore for at least 20 minutes prior to analysis to attain thermal equilibrium.

¹H NMR relaxation time measurements were performed using a standard $T_1 - T_2$ correlation pulse sequence,^[75] comprising an inversion recovery component followed by a CPMG echo train. For water-saturated zeolite systems the indirect (T_1) dimension was encoded using $m=32$ logarithmically spaced τ recovery times between 100 μs and 15 s, while the direction (T_2) dimension was acquired from the magnitude of $n=10,000$ spin echoes, separated by an echo time of $t_e=200$ μs. Each correlation measurement took approximately 1 hour to complete and included 8 repeat scans separated by a recycle delay of 15 s. For the measurement of bulk (unrestricted) water, the indirect dimension was encoded using $m=16$ logarithmically spaced τ recovery times between 1 ms and 30 s, while the direct dimension was acquired using $n=15,000$ echoes separated by $t_e=1$ ms; 4 repeat scans were employed separated by a recycle delay of 30 s, with the measurement taking approximately 20 minutes. In each case, the magnitude of each

echo $S(\tau, nt_e)$ was acquired as single data point with no spectral resolution.

The acquired NMR relaxation data may be described by a Fredholm integral equation of the first kind according to Eqn. 2,^[76]

$$\frac{S(\tau, nt_e)}{S(\infty, 0)} = \iint k(\tau, T_1, nt_e, T_2) F(T_1, T_2) d \log(T_1) d \log(T_2) + \varepsilon(\tau, nt_e). \quad (2)$$

Here, $S(\tau, nt_e)/S(\infty, 0)$ is the normalised echo magnitude, while $\varepsilon(\tau, nt_e)$ represents the noise, assumed Gaussian with zero mean. The function $K(\tau, T_1, nt_e, T_2)$ describes the expected form of the measured relaxation processes, with the form depicted in Eqn. 3,^[77]

$$K(\tau, T_1, nt_e, T_2) = \left[1 - 2 \exp\left(-\frac{\tau}{T_1}\right) \right] \exp\left(-\frac{nt_e}{T_2}\right). \quad (3)$$

Finally, $F(T_1, T_2)$ represents the desired 2D distribution of T_1 and T_2 relaxation time constants; distributions were obtained by applying a numerical inversion to the acquired NMR relaxation data according to the above expressions. Stability of the inverted distributions in the presence of noise was achieved through the use of Tikhonov regularisation,^[78] with the magnitude of the smoothing parameter chosen according to the Generalised Cross-validation method.^[51] The inversion algorithm was written in MATLAB (MathWorks Inc) and first implemented by Mitchell *et al.*^[79] and the resulting distributions were limited to (200×200) values within the range $\{10^{-4}, 10^1\}$ s.

¹H pulsed field gradient (PFG) NMR diffusion measurements were performed using the pulsed gradient stimulated echo (PGSTE) sequence.^[80] The self-diffusion coefficient D of water interacting with zeolite H-Y was obtained by fitting the acquired signal attenuation data to Eqn. 4,^[80]

$$\frac{S(g)}{S(0)} = \exp(-bD). \quad (4)$$

Here $S(0)$ is the NMR signal in the absence of any applied field gradient, while $S(g)$ is the corresponding signal in the presence of a gradient of magnitude g . The b -factor is obtained according to Eqn. 5,

$$b = \gamma^2 g^2 \delta^2 \left(\Delta - \frac{\delta}{3} \right), \quad (5)$$

where γ is the ¹H gyromagnetic ratio, while δ and Δ are the gradient pulse duration and observation time, respectively. To assess the diffusion of water within DA(HNO₃0.5 h)-Y, however, it was necessary to employ a bi-exponential fit of the form seen in Eqn. 6,

$$\frac{S(g)}{S(0)} = p_1 \exp(-bD_1) + p_2 \exp(-bD_2), \quad (6)$$

where the diffusion coefficients D_1 and D_2 describe signal attenuation rates at small and large b , respectively, while p_1 and p_2 indicate the relative populations characterised by these values. All PFG diffusion measurements were performed by holding $\delta = 1.5$ ms and $\Delta = 100$ ms constant while linearly varying g . Each measurement took approximately 1 hour to complete and included 8 repeat scans separated by a recycle delay of 15 s.

Catalytic cracking of 1,3,5-tipb in continuous flow

Cracking of 1,3,5-TIPB was performed in a continuous fixed-bed flow reactor at 1 bar. 0.1 g of catalyst was placed in a stainless steel reactor tube between quartz wool plugs and in thermal contact with a K-type thermocouple. Catalysts were activated in flowing N₂ (50 mL.min⁻¹) at 500 °C for 3 h, then cooled (20 °C.min⁻¹) to 350 °C. 1,3,5-triisopropylbenzene (95%, Sigma Aldrich) was then fed into N₂ stream at a liquid flow rate of 0.08 mL.min⁻¹ using a HPLC pump for 180 min. Reaction products were periodically passed through an ice-water bath to trap condensables, with a heated transfer line (150 °C) taking gaseous products for online analysis by a HP 5890 Series II gas chromatograph (GC) equipped with a flame ionisation detector (FID) and thermal conductor detector (TCD). Analysis was carried out in a series configuration over a Molesieve column connected to the TCD and a PLOT Q column connected to the FID (Table S2). A refinery gas standard containing C₁-C₆ molecules (RESTEK, Table S3) was used for calibration, with corresponding chromatograms shown in Figure S1. A schematic diagram of the reactor is shown in Figure S2. The reactor was purged with N₂ for 30 min before and after reactions. Qualitative and quantitative liquid products analyses were performed by an Agilent 6890GC and Shimadzu 2014GC-FID, respectively. 0.2 g of liquid product collected at different time-on-stream (TOS) was dissolved in 10 mL of dichloromethane (CH₂Cl₂, Sigma-Aldrich) to produce 2 mL aliquots for quantitative analysis over a Rtxi-1HT capillary column (15 m×0.25 mm×0.5 μm film thickness) using a He carrier gas, 1 μL sample injection and 150:1 split ratio. The GC oven was isothermal at 40 °C for 1 min, then ramped to 180 °C (15 °C.min⁻¹), with injector and detector temperatures of 260 °C and 280 °C respectively. For qualitative analysis, Agilent GC-6980MS equipped with an Rtx-200MS (30 m length, 0.25 mm ID, 0.5 μm film thickness) column was used. Sample injection volume and split ratio were kept at 1 μL and 100:1 respectively. Injector and detector temperatures were maintained at 220 °C and 285 °C respectively. The oven temperature was increased from 40 °C held for 5 min to 250 °C at a rate of 10 °C.min⁻¹. Liquid products including 1,3-diisopropylbenzene, 1,4-diisopropylbenzene, isopropylbenzene (IPB, cumene) and benzene were calibrated by analytical standards (Sigma-Aldrich) alongside 1,3,5-triisopropylbenzene.

Catalytic cracking of LDPE in continuous flow

Cracking of powdered LDPE (Alfa Aesar, <400 μm, melting point 104–138 °C) dissolved in toluene was carried out in the above continuous fixed-bed flow reactor under N₂ (100 mL.min⁻¹). Prior to reaction, the reactor was heated from 30–500 °C (ramp rate 10 °C.min⁻¹) for 3 h to activate the catalyst, and then cooled to 380 °C. LDPE dissolved in toluene (2 wt.%) was fed into a preheating zone using an HPLC pump, where it underwent vaporisation in the nitrogen stream. The weight hourly space velocity (WHSV) was 212 g_{LDPE/toluene}·g_{zeolite}⁻¹·h⁻¹. Reaction products were periodically passed through an ice-water bath to trap condensables. Gas and liquid products were analysed by GC as described above. Control experiments were performed with pure toluene to identify potential products from its conversion; under our reaction conditions, minimal C₅₋₆ paraffins or olefins were formed by toluene cracking, however liquid aromatic products of toluene disproportionation (benzene, toluene, ethylbenzene and xylenes) were observed. Carbon mass balances were calculated on a molar basis considering the products from LDPE cracking and pure toluene to eliminate possible solvent effects on LDPE cracking. Ultimate analysis of carbon, hydrogen and nitrogen for the virgin LDPE powder shown in Table S4 provided the precise composition for accurate mass balance calculation. Mass balances were >95% in all cases.

Conversion, product yield and selectivity for TIPB and LDPE cracking were calculated from Equations 7–11:

$$\text{TIPB conversion, } X_{\text{TIPB}} (\%) = \frac{\text{TIPB in feed} - \text{TIPB in product}}{\text{TIPB in feed}} \times 100 \quad (7)$$

$$\text{LDPE conversion, } X_{\text{LDPE}} (\%) = \frac{\text{total moles carbon in all products}}{\text{moles carbon in initial LDPE}} \times 100 \quad (8)$$

$$\text{Product selectivity, } S (\%) = \frac{\text{product yield}}{\text{TIPB conversion}} \times 100 \quad \text{or} \quad \frac{\text{carbon moles in product}}{\text{carbon moles in total products}} \times 100 \quad (9)$$

$$\text{Product yield, } Y (\%) = \frac{\text{moles carbon in product}}{\text{moles carbon in feedstream (or initial LDPE)}} \times 100 \quad (10)$$

$$\text{Weight hourly space velocity, } \text{WHSV} (h^{-1}) = \frac{\text{mass flow rate of feed}}{\text{mass of catalyst}} \quad (11)$$

Author Contributions

Jim Mensah: <https://www.rmit.edu.au/contact/staff-contacts/academic-staff/m/mensah-dr-jim> ORCID: 0000-0001-5388-9040; Penghui Yan: <https://chemeng.uq.edu.au/profile/5542/penghui-yan> ORCID: 0000-0002-5778-0509; Aditya Rawal: <https://www.analytical.unsw.edu.au/facilities/nmr-facility/staff-list/dr-aditya-rawal> ORCID: 0000-0002-5396-1265; Adam Lee: <https://experts.griffith.edu.au/41743-adam-lee> ; ORCID: 0000-0002-2153-1391; Karen Wilson: <https://experts.griffith.edu.au/42646-karen-wilson>; ORCID 0000-0003-4873-708X; Neil Robinson: <https://research-repository.uwa.edu.au/en/persons/neil-robinson> ORCID: 0000-0002-0893-2190; Michael Johns: <https://research-repository.uwa.edu.au/en/persons/michael-johns> ORCID: 0000-0001-7953-0597; Eric Kennedy: <https://www.newcastle.edu.au/profile/eric-kennedy>; Michael Stockenhuber: <https://www.newcastle.edu.au/profile/michael-stockenhuber> ORCID: 0000-0001-5026-2218

Acknowledgements

The authors thank the Australian Research Council (DP160102818, DP200103287, DP200100204, DP200100313 and LP190100849), and CRC-P (CRCPPEIGHT000194) for financial support. J. M. acknowledges the Electron Microscope and X-ray (EMX) unit and the Mark Wainwright Analytical Centre of the University of Newcastle and University of New South Wales respectively for access to their facilities. N. R. acknowledges support from the Forrest Research Foundation. Open Access publishing facilitated by The University of Newcastle, as part of the Wiley - The University of Newcastle agreement via the Council of Australian University Librarians.

Conflict of Interests

The authors declare no competing financial interest.

Data Availability Statement

The data that support the findings of this study are available on request from the corresponding author. The data are not publicly available due to privacy or ethical restrictions.

Keywords: acidity · cracking · mesopores · micropores · zeolites

- [1] R. Geyer, J. R. Jambeck, K. L. Law, *Sci. Adv.* **2017**, *3*.
- [2] D. P. Serrano, J. Aguado, J. M. Escola, *ACS Catal.* **2012**, *2*, 1924–1941.
- [3] a) P. T. Williams, E. A. Williams, *Energy Fuels* **1999**, *13*, 188–196; b) J. Walendziewski, M. Steining, *Catal. Today* **2001**, *65*, 323–330.
- [4] A. Corma, *Chem. Rev.* **1995**, *95*, 559–614.
- [5] J. Aguado, D. P. Serrano, J. L. Sotelo, R. Van Grieken, J. M. Escola, *Ind. Eng. Chem. Res.* **2001**, *40*, 5696–5704.
- [6] G. Manos, A. Garforth, J. Dwyer, *Ind. Eng. Chem. Res.* **2000**, *39*, 1198–1202.
- [7] A. Garforth, Y.-H. Lin, P. Sharratt, J. Dwyer, *Appl. Catal., A* **1998**, *169*, 331–342.
- [8] S. Al-Khattaf, H. De Lasa, *Appl. Catal., A* **2002**, *226*, 139–153.
- [9] M. A. Ardagh, Z. Bo, S. L. Nauert, J. M. Notestein, *ACS Catal.* **2016**, *6*, 6156–6164.
- [10] a) M. Davoodpour, R. Tafreshi, A. A. Khodadadi, Y. Mortazavi, *Korean J. Chem. Eng.* **2017**, *34*, 681–691; b) J. Zhao, L. Q. Yang, L. Yu, X. M. Zhao, Y. C. Hao, Z. J. Zhao, *Dig. J. Nano. & Bio.* **2021**, *16*, 17.
- [11] A. Bazyari, A. Khodadadi, N. Hosseinpour, Y. Mortazavi, *Fuel Process. Technol.* **2009**, *90*, 1226–1233.
- [12] K. A. Tarach, K. Gora-Marek, J. Martinez-Triguero, I. Melian-Cabrera, *Catal. Sci. and Technol.* **2017**, *7*, 858–873.
- [13] M. H. Sun, L. H. Chen, S. Yu, Y. Li, X. G. Zhou, Z. Y. Hu, Y. H. Sun, Y. Xu, B. L. Su, *Angew. Chem., Int. Ed.* **2020**, *44*, 19750–19759.
- [14] J. Mensah, P. Yan, E. Kennedy, M. Drewery, M. Stockenhuber, *Microporous Mesoporous Mater.* **2021**, *328*, 111399.
- [15] a) J. Perez-Ramirez, C. H. Christensen, K. Egeblad, C. H. Christensen, J. C. Groen, *Chem. Soc. Rev.* **2008**, *37*, 2530–2542; b) M. S. Holm, E. Taarning, K. Egeblad, C. H. Christensen, *Catal. Today* **2011**, *168*, 3–16; c) K. Li, J. Valla, J. Garcia-Martinez, *ChemCatChem* **2014**, *6*, 46–66.
- [16] W. O. Haag, R. M. Lago, P. B. Weisz, *Faraday Discuss. Chem. Soc.* **1981**, *72*, 317–330.
- [17] K. Rajagopalan, A. Peters, G. Edwards, *Appl. Catal.* **1986**, *23*, 69–80.
- [18] E. A. Swabb, B. C. Gates, *Ind. Eng. Chem. Fundam.* **1972**, *11*, 540–545.
- [19] G. Bellussi, G. Pazzucconi, C. Perego, G. Girotti, G. Terzoni, *J. Catal.* **1995**, *157*, 227–234.
- [20] a) D. McQueen, B. H. Chiche, F. Fajula, A. Auroux, C. Guimon, F. Fitoussi, P. Schulz, *J. Catal.* **1996**, *161*, 587–596; b) A. Boréave, A. Auroux, C. Guimon, *Microporous Mater.* **1997**, *11*, 275–291.
- [21] a) A. H. Janssen, A. J. Koster, K. P. de Jong, *J. Phys. Chem. B* **2002**, *106*, 11905–11909; b) A. H. Janssen, A. J. Koster, K. P. de Jong, *Angew. Chem., Int. Ed.* **2001**, *40*, 1102–1104.
- [22] R. López-Fonseca, B. de Rivas, J. Gutiérrez-Ortiz, J. González-Velasco, in *Stud. Surf. Sci. Catalysis, Vol. 144*, Elsevier, **2002**, pp. 717–722.
- [23] Y. Tao, H. Kanoh, L. Abrams, K. Kaneko, *Chem. Rev.* **2006**, *106*, 896–910.
- [24] C. S. Triantafyllidis, A. G. Vlessidis, N. P. Evmiridis, *Ind. Eng. Chem. Res.* **2000**, *39*, 307–319.
- [25] P. Kortunov, S. Vasenkov, J. Kärger, R. Valiullin, P. Gottschalk, M. Fé Elía, M. Perez, M. Stöcker, B. Drescher, G. McElhiney, *J. Am. Chem. Soc.* **2005**, *127*, 13055–13059.
- [26] D. Verboekend, N. Nuttens, R. Locus, J. Van Aelst, P. Verolme, J. C. Groen, J. Perez-Ramirez, B. F. Sels, *Chem. Soc. Rev.* **2016**, *45*, 3331–3352.
- [27] D. Verboekend, G. Vilé, J. Pérez-Ramirez, *Adv. Funct. Mater.* **2012**, *22*, 916–928.
- [28] a) J. Rouquerol, P. Llewellyn, F. Rouquerol, in *Stud. Surf. Sci. Catalysis, Vol. 160* (Eds.: P. L. Llewellyn, F. Rodriguez-Reinoso, J. Rouquerol, N. Seaton), Elsevier, **2007**, pp. 49–56; b) K. S. Sing, D. H. Everett, R. Haul, L.

- Moscou, R. A. Pierotti, J. Rouquerol, T. Siemieniowska, *Pure Appl. Chem.* **1985**, *57*, 603–619.
- [29] K. A. Cychosz, R. Guillet-Nicolas, J. García-Martínez, M. Thommes, *Chem. Soc. Rev.* **2017**, *46*, 389–414.
- [30] A. de Lucas, J. L. Valverde, P. Sánchez, F. Dorado, M. J. Ramos, *Appl. Catal., A* **2005**, *282*, 15–24.
- [31] a) M. Pan, J. Zheng, Y. Liu, W. Ning, H. Tian, R. Li, *J. Catal.* **2019**, *369*, 72–85; b) Z. Qin, B. Shen, X. Gao, F. Lin, B. Wang, C. Xu, *J. Catal.* **2011**, *278*, 266–275.
- [32] S. C. Cardona, A. Corma, *Appl. Catal., B* **2000**, *25*, 151–162.
- [33] B. Xu, C. Sievers, S. B. Hong, R. Prins, J. A. van Bokhoven, *J. Catal.* **2006**, *244*, 163–168.
- [34] S. Kotrel, M. P. Rosynek, J. H. Lunsford, *J. Catal.* **1999**, *182*, 278–281.
- [35] B. Xu, S. Bordiga, R. Prins, J. A. van Bokhoven, *Appl. Catal., A* **2007**, *333*, 245–253.
- [36] L. H. Ong, M. Dömök, R. Olindo, A. C. van Veen, J. A. Lercher, *Microporous Mesoporous Mater.* **2012**, *164*, 9–20.
- [37] H. G. Karge, M. Hunger, H. K. Beyer, in *Catal. Zeolites: Fundamentals and Applications* (Eds.: J. Weitkamp, L. Puppe), Springer Berlin Heidelberg, Berlin, Heidelberg, **1999**, pp. 198–326.
- [38] A. W. Chester, E. G. Derouane, *Zeolite characterization and catalysis*, Springer, **2009**.
- [39] a) M. Boronat, A. Corma, *Catal. Lett.* **2015**, *145*, 162–172; b) R. A. van Santen, G. J. Kramer, *Chem. Rev.* **1995**, *95*, 637–660.
- [40] a) M. S. Holm, S. Svelle, F. Joensen, P. Beato, C. H. Christensen, S. Bordiga, M. Bjørgen, *Appl. Catal., A* **2009**, *356*, 23–30; b) X. Pu, N.-W. Liu, L. Shi, *Microporous Mesoporous Mater.* **2015**, *201*, 17–23.
- [41] S. Mitchell, M. Milina, R. Verel, M. Hernandez-Rodriguez, A. B. Pinar, L. B. McCusker, J. Perez-Ramirez, *Chem.-Eur. J.* **2015**, *21*, 14156–14164.
- [42] a) K. Góra-Marek, M. Derewiński, P. Sarv, J. Datka, *Catal. Today* **2005**, *101*, 131–138; b) F. Lónyi, J. H. Lunsford, *J. Catal.* **1992**, *136*, 566–577; c) in *Zeolites Catal.*, **2010**, pp. 283–300.
- [43] M. Stockenhuber, J. A. Lercher, *Microporous Mater.* **1995**, *3*, 457–465.
- [44] J. Datka, B. Gil, T. Domagała, K. Góra-Marek, *Microporous Mesoporous Mater.* **2001**, *47*, 61–66.
- [45] C. Bisio, G. Martra, S. Coluccia, P. Massiani, *J. Phys. Chem. C* **2008**, *112*, 10520–10530.
- [46] V. C. dos Santos, K. Wilson, A. F. Lee, S. Nakagaki, *Appl. Catal., B* **2015**, *162*, 75–84.
- [47] N. Bloembergen, E. M. Purcell, R. V. Pound, *Phys. Rev.* **1948**, *73*, 679.
- [48] N. Robinson, C. Robertson, L. F. Gladden, S. J. Jenkins, C. D'Agostino, *ChemPhysChem* **2018**, *19*, 2472–2479.
- [49] N. Robinson, P. Bräuer, A. P. York, C. D'Agostino, *Phys. Chem. Chem. Phys.* **2021**, *23*, 17752–17760.
- [50] N. Robinson, E. F. May, M. L. Johns, *ACS Appl. Mater. Interfaces* **2021**, *13*, 54476–54485.
- [51] J. Mitchell, T. Chandrasekera, L. Gladden, *Prog. Nucl. Magn. Reson. Spectrosc.* **2012**, *62*, 34–50.
- [52] D. Bernin, D. Topgaard, *Curr. Opin. Colloid Interface Sci.* **2013**, *18*, 166–172.
- [53] J. Kärger, M. Avramovska, D. Freude, J. Haase, S. Hwang, R. Valiullin, *Adsorption* **2021**, *27*, 453–484.
- [54] N. Robinson, C. D'Agostino, *Top. Catal.* **2020**, *63*, 319–327.
- [55] M. S. Aghakhani, A. A. Khodadadi, S. Najafi, Y. Mortazavi, *J. Ind. Eng. Chem.* **2014**, *20*, 3037–3045.
- [56] S. Al-Khattaf, J. A. Atias, K. Jarosch, H. de Lasa, *Chem. Eng. Sci.* **2002**, *57*, 4909–4920.
- [57] S. Al-Khattaf, H. de Lasa, *Appl. Catal., A* **2002**, *226*, 139–153.
- [58] a) N. Hosseinpour, A. A. Khodadadi, Y. Mortazavi, A. Bazyari, *Appl. Catal., A* **2009**, *353*, 271–281; b) N. Hosseinpour, Y. Mortazavi, A. Bazyari, A. A. Khodadadi, *Fuel Process. Technol.* **2009**, *90*, 171–179.
- [59] A. Sanchez, S. Ramirez, W. Silva, J. F. Espinal, *Mol. Catal.* **2019**, *466*, 13–18.
- [60] G. Xiong, S. Zhou, L. Liu, J. Qian, J. Liu, L. Zhao, *Eur. J. Inorg. Chem.* **2022**, *2022*, e202200260.
- [61] N. T. Ramirez-Marquez, D. J. Pérez-Martínez, C.-A. Trujillo, *Microporous Mesoporous Mater.* **2023**, *360*, 112700.
- [62] X. H. Vu, T. T. Truong, U. Armbruster, *J. Porous Mater.* **2019**, *26*, 175–184.
- [63] A. Corma, B. Wojciechowski, *Catal. Rev. Sci. Eng.* **1982**, *24*, 1–65.
- [64] G. de la Puente, C. Klocker, U. Sedran, *Appl. Catal., B* **2002**, *36*, 279–285.
- [65] P. N. Sharratt, Y. H. Lin, A. A. Garforth, J. Dwyer, *Ind. Eng. Chem. Res.* **1997**, *36*, 5118–5124.
- [66] D. Park, E. Hwang, J. Kim, J. Choi, Y. Kim, H. Woo, *Polym. Degrad. Stab.* **1999**, *65*, 193–198.
- [67] R. P. Lattimer, *J. Anal. Appl. Pyrolysis* **1995**, *31*, 203–225.
- [68] A. Peral, J. M. Escola, D. P. Serrano, J. Pěch, C. Ochoa-Hernández, J. Čejka, *Catal. Sci. Technol.* **2016**, *6*, 2754–2765.
- [69] D. Jampaiah, D. Y. Murzin, A. F. Lee, D. Schaller, S. K. Bhargava, B. Tabulo, K. Wilson, *Energy Environ. Sci.* **2022**, *15*, 1760–1804.
- [70] D. Zhao, J. Feng, Q. Huo, N. Melosh, G. H. Fredrickson, B. F. Chmelka, G. D. Stucky, *Science* **1998**, *279*, 548–552.
- [71] S. Zeng, J. Blanchard, M. Breyse, Y. Shi, X. Shu, H. Nie, D. Li, *Microporous Mesoporous Mater.* **2005**, *85*, 297–304.
- [72] P. Yan, J. Mensah, A. Adesina, E. Kennedy, M. Stockenhuber, *Appl. Catal., B* **2020**, *267*, 118690.
- [73] M. L. Bonati, R. W. Joyner, M. Stockenhuber, *Catal. today* **2003**, *81*, 653–658.
- [74] a) K. Góra-Marek, K. Brylewska, K. A. Tarach, M. Rutkowska, M. Jabłońska, M. Choi, L. Chmielarz, *Appl. Catal., B* **2015**, *179*, 589–598; b) T. Barzetti, E. Selli, D. Moscotti, L. Forni, *J. Chem. Soc., Faraday Trans.* **1996**, *92*, 1401–1407.
- [75] Y.-Q. Song, L. Venkataramanan, M. Hürlimann, M. Flaum, P. Frulla, C. Straley, *J. Magn. Reson.* **2002**, *154*, 261–268.
- [76] L. Venkataramanan, Y.-Q. Song, M. D. Hürlimann, *EEE Trans. Signal Process.* **2002**, *50*, 1017–1026.
- [77] J. Mitchell, L. Gladden, T. Chandrasekera, E. Fordham, *Prog. Nucl. Magn. Reson. Spectrosc.* **2014**, *76*, 1–60.
- [78] A. N. Tikhonov, V. Arsenin, (*Solutions of ill-posed problems*) **1977**, Vol. 14.
- [79] J. Mitchell, D. G. von der Schulenburg, D. Holland, E. Fordham, M. Johns, L. Gladden, *J. Magn. Reson.* **2008**, *193*, 218–225.
- [80] E. O. Stejskal, J. E. Tanner, *J. Chem. Phys.* **1965**, *42*, 288–292.

Manuscript received: July 14, 2023

Revised manuscript received: November 8, 2023

Accepted manuscript online: November 15, 2023

Version of record online: December 27, 2023